Exp. Theo. NANOTECHNOLOGY 10 (2026) 343-356 https://doi.org/10.56053/10.S.343

Enhancing α-Bi_2O_3 nanoparticle crystallinity and antibacterial functionality through controlled calcination

Zahraa Salah Ahmed[1], *Mohammed RASHEED*[2,*], *Hayder S. Ahmed*[3]

[1]Applied Sciences Department, University of Technology- Iraq, Baghdad 10066, Iraq
[2]College of Production Engineering & Metallurgy, University of Technology- Iraq, Baghdad, Iraq
[3]Electronic and Communication Department, Engineering College, University of Baghdad, Iraq
[*]) Email: rasheed.mohammed40@yahoo.com

Received 17/11/2025, *Received in revised form* 15/12/2025, *Accepted* 28/12/2025, *Published* 15/2/2026

This study examines the effect of calcination temperature on the structural, vibrational, magnetic, and antibacterial properties of α-Bi_2O_3 pellets synthesized at 300, 400, and 500 °C. XRD analysis confirmed the formation of a single-phase monoclinic α-Bi_2O_3 structure (JCPDS No. 71-0465) for all samples, with enhanced crystallinity at higher temperatures, evidenced by reduced FWHM, increased crystallite size (267.83 to 373.65 nm), and decreased micro-strain and dislocation density. FTIR spectra showed characteristic Bi–O vibrational modes with increased sharpness and intensity at elevated calcination temperatures, indicating improved structural ordering. VSM measurements for the sample calcined at 500 °C revealed weak ferromagnetic behavior with soft magnetic characteristics, exhibiting low coercivity (~150), small remanent magnetization (~0.020 emu g^{-1}), and a maximum magnetization of ~0.060 emu g^{-1}, attributed to defect- and surface-induced magnetism. Antibacterial studies against *E. coli* and *S. aureus* demonstrated enhanced efficacy at 500 °C, particularly against *E. coli*, confirming that higher calcination temperatures significantly improve the multifunctional performance of α-Bi_2O_3.

Keywords: α-Bi_2O_3; FTIR; XRD; Antibacterial.

1. INTRODUCTION

Bismuth oxide (α-Bi_2O_3) is a technologically important metal oxide that has attracted significant interest due to its versatile physicochemical properties and broad range of applications [1-5]. It possesses a high refractive index, large dielectric permittivity, narrow band gap, and strong photoconductive behavior, making it suitable for optoelectronic devices, photocatalysis, solid oxide fuel cells (SOFCs), and gas sensing applications [6,7]. Moreover, its non-toxicity and environmental compatibility make Bi_2O_3 a promising alternative to many conventional transition metal oxides, especially for biomedical and sustainable technologies [8,9]. Bi_2O_3 is polymorphic in nature and can exist in monoclinic (α), tetragonal (β), cubic (δ), and body-centered cubic (γ) phases, among which the monoclinic α-phase is the most stable at room temperature and therefore widely explored for practical applications [10,11]. In recent years, nanostructured Bi_2O_3 has gained growing attention because materials at the nanoscale often exhibit properties that differ markedly from their bulk counterparts [12-14]. The reduction in particle size leads to an increased surface-to-volume ratio and quantum confinement effects, which can significantly enhance catalytic activity, sensing performance, optical absorption, and energy storage efficiency [15,16]. Bi_2O_3 nanoparticles have shown excellent visible-light-driven photocatalytic activity for the degradation of organic pollutants, high sensitivity toward toxic gases such as NO_2 and CO, and improved electrochemical performance when incorporated into battery electrodes [17-20]. Achieving optimal performance in these applications requires precise control over nano-structural parameters such as particle size, crystallinity, morphology, and phase purity [21, 22]. The functional behavior of Bi_2O_3 nanoparticles is strongly governed by their nanostructure [23, 24]. Parameters such as crystallite size, defect density, phase composition, and morphology directly influence charge transport, surface reactivity, optical properties, and ionic conductivity [25, 26]. For instance, nanostructuring can modify the band gap energy, thereby affecting light absorption in photocatalytic and photovoltaic applications, while increased defect density can enhance charge separation and transport [27,28]. Additionally, the specific crystalline phase of Bi_2O_3 plays a critical role in determining its electrical and ionic conductivity, which is essential for applications in electrochemical and sensing devices. Various synthesis routes, including sol–gel, hydrothermal, precipitation, combustion, and microwave-assisted methods, have been employed to produce Bi_2O_3 nanostructures [29,30]. Among these, the sol–gel method is particularly attractive due to its simplicity, low cost, scalability, low processing temperature, and excellent control over stoichiometry and homogeneity [31,32]. In this study, α-Bi_2O_3 nanoparticles are synthesized using the sol–gel route, and their structural and bonding characteristics are systematically investigated using X-ray diffraction (XRD) and Fourier-transform infrared spectroscopy (FTIR). The primary objective is to establish a clear relationship between synthesis conditions and nano-structural features, thereby supporting the development of high-quality, efficient, and environmentally friendly Bi_2O_3-based materials for advanced technological applications.

2. MATERIALS AND METHODS

2.1 Chemicals and reagents

The main precursor for bismuth oxide (Bi_2O_3) in the sol–gel reaction is bismuth nitrate pentahydrate [$Bi(NO_3)_3 \cdot 5H_2O$], which serves as a rich source of Bi^{3+} ions essential for Bi_2O_3 formation. All chemicals are of analytical grade and ≥99% purity, used as received without further purification to avoid contamination and maintain the uniformity of the synthesis. To promote homogeneous metal ion distribution and stabilize the sol, citric acid monohydrate ($C_6H_8O_7 \cdot H_2O$) is employed as a chelating and fuel agent. Its strong complexation with Bi^{3+} ions control the gelation rate and prevents premature precipitation, while also aiding the combustion process during calcination, resulting in improved crystallinity. Distilled water is used as the solvent for dissolving the metal precursor and citric acid. No external pH adjustment is performed; the natural acidity from citric acid is sufficient to promote controlled hydrolysis and condensation reactions. All chemicals are sourced from reliable suppliers such as Merck or Sigma-Aldrich.

2.2 Sol–gel synthesis procedure

The structural, vibrational, magnetic, and antibacterial properties of the synthesized Bi_2O_3 nanoparticles are systematically investigated using X-ray diffraction (XRD), Fourier-transform infrared (FTIR) spectroscopy, vibrating sample magnetometry (VSM), and microbiological assays. XRD analysis is performed using a Bruker D8 Advance diffractometer with Cu Kα radiation (λ = 1.5406 Å) operated at 40 kV and 40 mA, recording diffraction patterns over a 2θ range of 20°–80° to identify crystalline phases and evaluate microstructural parameters such as crystallite size, micro-strain, and dislocation density using the Scherrer and Williamson–Hall methods. FTIR spectra are collected using a Bruker Tensor 27 spectrometer in the 4000–400 cm^{-1} range at a resolution of 4 cm^{-1} to analyze Bi–O vibrational modes and confirm the removal of organic residues after calcination. Magnetic properties are examined at room temperature using a vibrating sample magnetometer (VSM) by recording magnetization–field (M–H) hysteresis loops over an applied magnetic field range of ±10 kOe, allowing determination of key magnetic parameters including saturation magnetization, remanent magnetization, coercivity, and squareness ratio. Antibacterial activity is assessed against *Escherichia coli* and *Staphylococcus aureus* using the Agar Diffusion Method (ADM) and Spread Plate Method (SPM), with inhibition zones and viable colony counts measured after 24 h incubation at 37 °C. All measurements are conducted in triplicate, enabling reliable correlation between structural, magnetic, and antibacterial properties.

3 RESULTS AND DISCUSSION

3.1 XRD analysis

3.1.1 Phase identification and crystal structure

Figure 1 presents the X-ray diffraction (XRD) patterns of Bi_2O_3 powders calcined at 350, 400, and 500 °C. All diffraction peaks are sharp and well-defined, corresponding to the characteristic planes of monoclinic α-Bi_2O_3, in agreement with the standard JCPDS card No. 71-0465. The absence of extra peaks confirms the high phase purity of the synthesized powders. As the calcination temperature increases, the diffraction peaks become narrower and more intense, reflecting reduced peak broadening and improved crystallinity, which is directly associated with an increase in crystallite size [33-35]. The average interplanar spacing d for each peak is calculated using Bragg's law [36-40]:

$$d = \frac{\lambda}{2sin\theta} \tag{1}$$

where λ is the X-ray wavelength (1.5406 Å for Cu Kα radiation) and θ is half of the measured 2θ/2 value. The crystallite size *D* is estimated from the Debye–Scherrer equation [41, 42]:

$$D = \frac{K\lambda}{\beta cos\theta} \tag{2}$$

where K is the shape factor (0.9), β is the full width at half maximum (FWHM) of the peak in radians, and θ is the Bragg angle. The results show that D increases from lower to higher calcination temperatures, reflecting enhanced grain growth upon thermal treatment. The microstrain (ε) is obtained from [43, 44]:

$$\varepsilon = \frac{\beta}{4tan\theta} \tag{3}$$

and the dislocation density (δ) is determined using [45, 46]:

$$\delta = \frac{1}{D^2} \tag{4}$$

where D is in nm, δ is in m^{-2}. The cubic lattice parameters are refined using [47, 48]:

$$a = d\sqrt{h^2 + k^2 + l^2} \tag{5}$$

yielding values consistent with the standard α-Bi_2O_3 phase. Overall, increasing calcination temperature enhances crystallinity, enlarges crystallite size, and reduces internal strain, all of which are essential for optimizing the functional performance of Bi_2O_3 in catalytic, sensing, and optoelectronic application. Yielding refined lattice parameters consistent with the monoclinic α-Bi_2O_3 phase ($a \approx 5.848$ Å, $b \approx 8.169$ Å, $c \approx 7.510$ Å, $\beta \approx 112.96°$), in agreement with the standard JCPDS card No. 71-0465 [49-51].

Table 1 summarizes the XRD-derived structural parameters of Bi_2O_3 powders calcined at 300, 400, and 500 °C. All diffraction peaks correspond to the monoclinic α-Bi_2O_3 phase (JCPDS No. 71-0465), confirming phase purity at all calcination temperatures. A systematic decrease in the full width at half maximum (FWHM) from ~0.325° at 300 °C to ~0.278° at 400 °C and ~0.233° at 500 °C indicates progressive improvement in crystallinity and reduced lattice imperfections with increasing temperature. The crystallite size, calculated using the Debye–Scherrer equation, increases significantly from 267.83 nm at 300 °C to 305.47 nm at 400 °C and reaches 373.65 nm at 500 °C, reflecting thermally driven grain growth due to enhanced atomic diffusion. Correspondingly, microstrain decreases from 3.687×10^{-3} to 2.637×10^{-3}, while dislocation density drops from $\sim 0.14 \times 10^{14}$ m^{-2} to $\sim 0.07 \times 10^{14}$ m^{-2}, indicating effective relaxation of lattice distortions and reduction of crystal defects. Overall, increasing calcination temperature markedly enhances crystal quality, reduces defect density, and promotes superior structural stability in Bi_2O_3 powders [52-54].

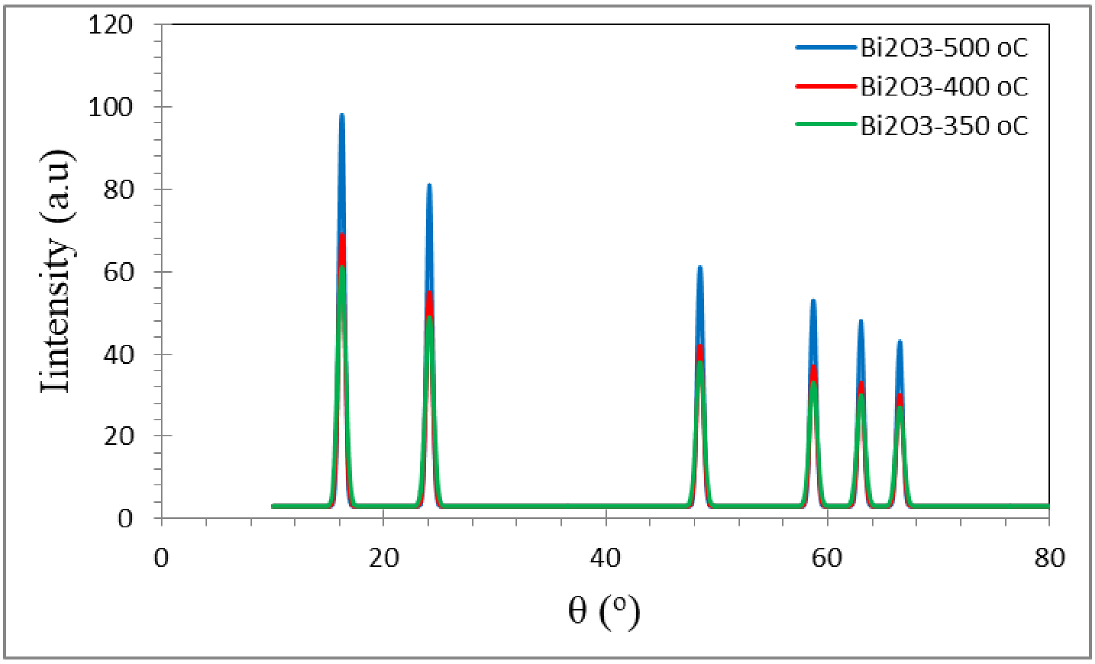

Figure 1 XRD patterns of α-Bi_2O_3 pellets calcined at 300, 400, and 500 °C.

Table 1 Structural parameters of Bi_2O_3 powders calcined at 300, 400, and 500 °C.

Samples	2Theata	(hkl)	FWHM (°)	d-Spacing (A)	D (nm)	**ε**	***δ*** $(m)^{-2}$
Bi_2O_3-300 °C	27.9	(120)	0.310	3.195270	264.06	0.005445	0.14
	33.2	(121)	0.315	2.696295	263.17	0.00461	0.14
	46.3	(041)	0.320	1.959355	270.00	0.003266	0.14
	55.5	(002)	0.335	1.654373	267.96	0.002778	0.14
	65.6	(240)	0.345	1.421983	273.95	0.002336	0.13
Average					267.83	0.003687	0.14
Bi_2O_3-400 °C	27.9	(120)	0.270	3.195270	303.17	0.004743	0.11
	33.2	(121)	0.275	2.696295	301.45	0.004025	0.11
	46.3	(041)	0.280	1.959355	308.57	0.002857	0.11
	55.5	(002)	0.295	1.654373	304.30	0.002447	0.11
	65.6	(240)	0.305	1.421983	309.87	0.002065	0.1
Average					305.47	0.003227	0.11
Bi_2O_3-500 °C	27.9	(120)	0.220	3.195270	372.08	0.003864	0.07
	33.2	(121)	0.225	2.696295	368.43	0.003293	0.07
	46.3	(041)	0.230	1.959355	375.65	0.002347	0.07
	55.5	(002)	0.240	1.654373	374.03	0.00199	0.07
	65.6	(240)	0.250	1.421983	378.04	0.001693	0.07
Average					373.65	0.002637	0.07

Figure 2 presents the evolution of microstructural parameters of Bi_2O_3 samples calcined at 350, 400, and 500 °C, clearly demonstrating the effect of calcination temperature on structural quality. The FWHM decreases from 0.325° at 350 °C to 0.233° at 500 °C, indicating progressive peak narrowing associated with enhanced crystallinity and reduced structural disorder. Correspondingly, the crystallite size increases markedly from 267.83 nm to 373.65 nm, reflecting thermally induced grain coarsening facilitated by increased atomic diffusion at higher temperatures. Microstrain decreases from 3.687×10^{-3} to 2.637×10^{-3}, signifying relaxation of lattice distortions and defect annihilation during calcination. Similarly, the dislocation density drops from 0.14×10^{14} m^{-2} to 0.07×10^{14} m^{-2}, consistent with crystallite growth and reduced defect concentration. Overall, increasing the calcination temperature from 350 °C to 500 °C results in improved structural order, larger crystallites, and significantly lower lattice strain and dislocation density, which are essential for achieving high-performance Bi_2O_3-based functional materials [55-60].

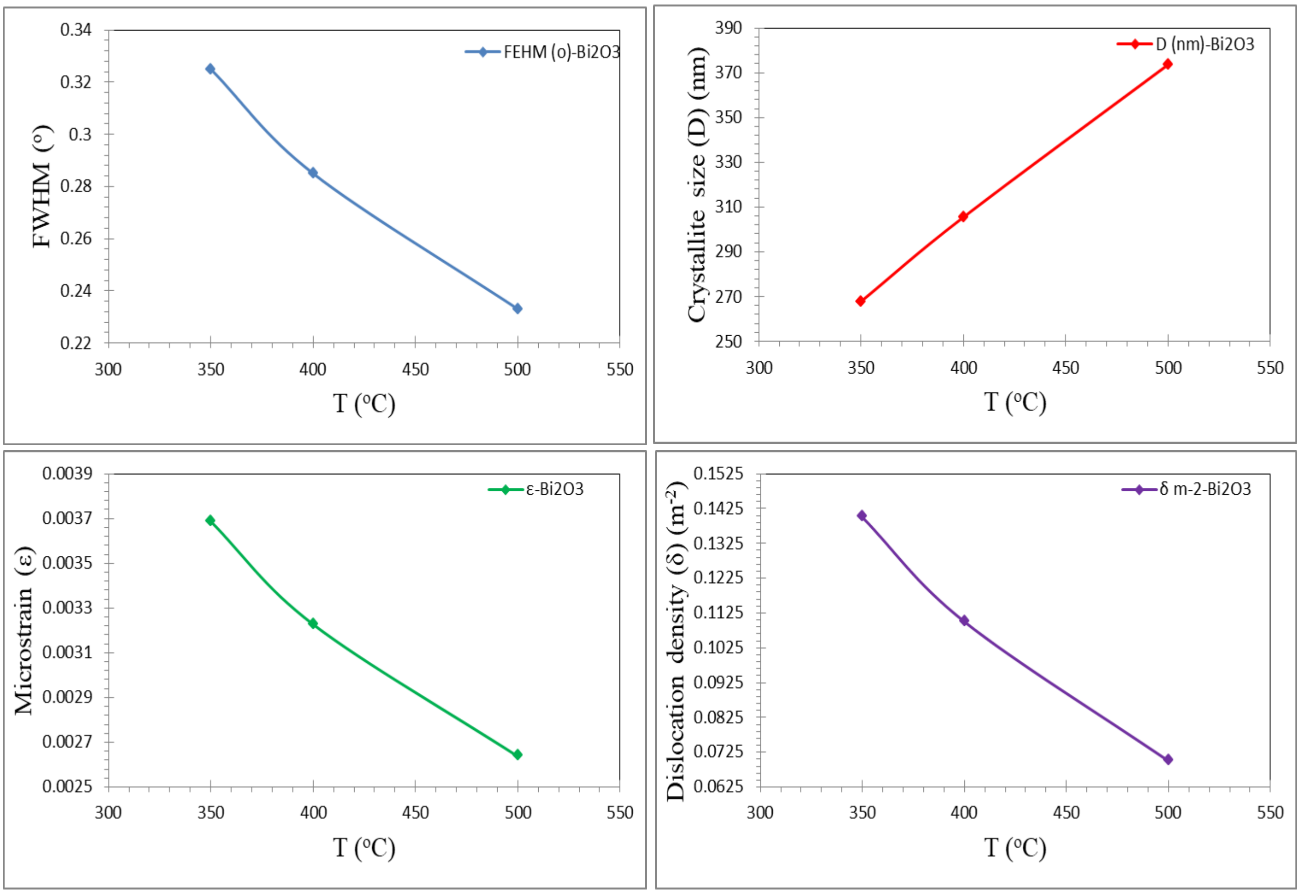

Figure 2 Variation of average crystallite size (D), microstrain (ε), and dislocation density (δ) of α-Bi_2O_3 samples calcined at 350, 400, and 500 °C, as calculated from XRD data using the Debye–Scherrer and Williamson–Hall methods.

3.2 FTIR analysis

3.2.1 Identification of functional groups

Figure 3 presents the FTIR transmittance spectra of α-Bi_2O_3 samples calcined at 350, 400, and 500 °C in the range of 400–4000 cm^{-1}. Strong absorption bands observed in the 400–800 cm^{-1} region correspond to Bi–O stretching vibrations, confirming the formation of the monoclinic α-Bi_2O_3 lattice. The intensity of these bands increases with calcination temperature, indicating improved crystallinity and reduced structural disorder, in agreement with XRD results. Weak features in the 800–1500 cm^{-1} region are attributed to residual carbonate species or minor lattice vibrations, whose diminishing intensity at higher temperatures suggests effective precursor decomposition. Bands around 1500–1700 cm^{-1} and the broad region at 3200–3600 cm^{-1} are associated with H–O–H bending and O–H stretching vibrations of adsorbed water and hydroxyl groups; their reduced intensity at 500 °C confirms the removal of surface-adsorbed species. Overall transmittance decreases with increasing calcination temperature, likely due to grain growth, densification, and enhanced light scattering. These results confirm enhanced structural purity and thermal stabilization of α-Bi_2O_3 at higher calcination temperatures [61-63].

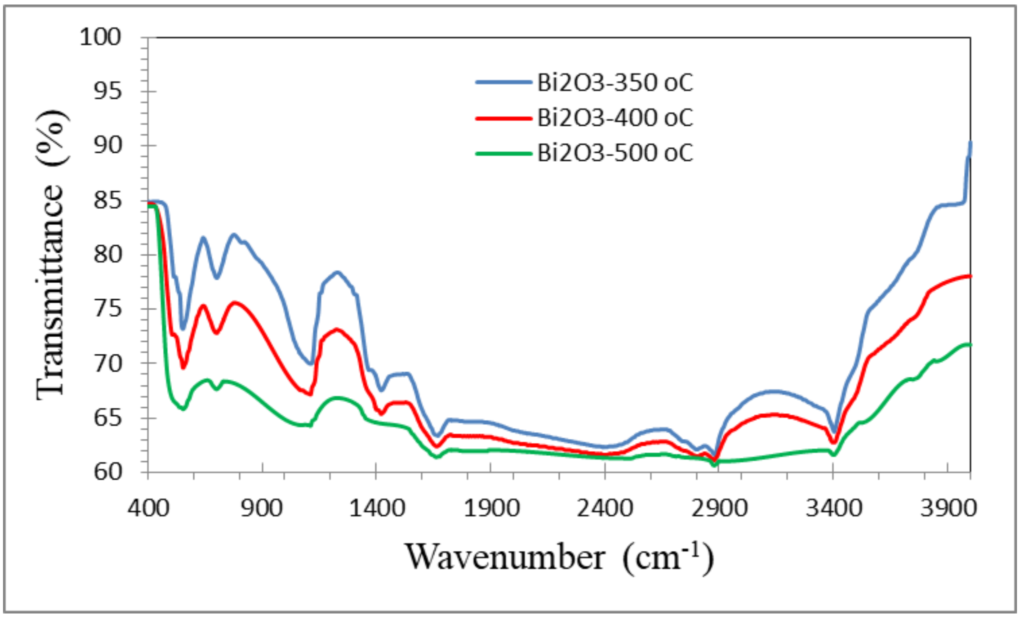

Figure 3 FTIR spectra of α-Bi_2O_3 pellets calcined at 350, 400, and 500 °C.

3.3 VSM

The VSM (M–H) hysteresis curve of Bi_2O_3 nanoparticles calcined at 500 °C displays a very narrow loop centered near the origin, indicating weak magnetic ordering with soft-magnetic behavior. The magnetization rises sharply at low applied fields, reflecting easy magnetization, and then gradually approaches a nearly constant value at higher fields without clear saturation, which is typical of defect-mediated magnetic systems. The maximum magnetization reaches approximately +0.060 emu g^{-1} at positive high field and −0.060 emu g^{-1} at the corresponding negative field. The remanent magnetization is relatively small, with values of about ±0.020 emu g^{-1}, showing that only a minor fraction of magnetization is retained after removal of the external field. The coercive field is low, around ±150, indicating minimal resistance to magnetization reversal. These features confirm the soft magnetic nature and weak ferromagnetic characteristics of the Bi_2O_3 nanoparticles. The observed magnetic behavior is attributed to oxygen vacancies, lattice defects, and uncompensated surface spins introduced during nanoparticle synthesis and thermal treatment, with calcination at 500 °C enhancing crystallinity while preserving defect-induced magnetism [64-66].

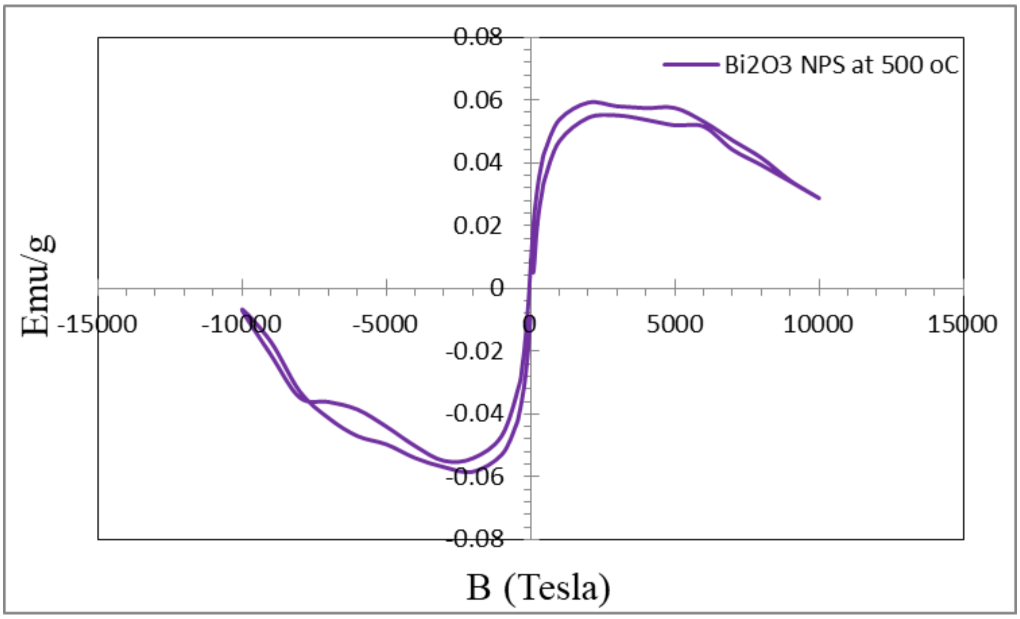

Figure 4 Room-temperature VSM hysteresis (M–H) loop of Bi_2O_3 nanoparticles calcined at 500 °C.

3.4 Antibacterial activity

3.4.1 ADM

The antibacterial activity of the α-Bi_2O_3 pellet calcined at 500 °C is evaluated against *Staphylococcus aureus* (Gram-positive) and *Escherichia coli* (Gram-negative) using the agar diffusion method. The measured inhibition zone diameters are 8 mm for *S. aureus* and 9 mm for *E. coli*, confirming that the calcined α-Bi_2O_3 pellet exhibits effective antibacterial activity against both bacterial strains, with slightly higher efficacy toward the Gram-negative bacterium. This difference can be attributed to variations in cell wall structure between the two bacteria. Gram-negative bacteria possess an outer membrane containing lipopolysaccharides, which can be more susceptible to reactive oxygen species (ROS) generated on the Bi_2O_3 surface and to ionic interactions. In contrast, the thicker peptidoglycan layer of Gram-positive bacteria provides greater resistance to surface interactions. Calcination at 500 °C enhances crystallinity and optimizes surface chemistry, which likely promotes ROS generation and improves bacterial contact. These results demonstrate that α-Bi_2O_3 retains antibacterial functionality in pellet form and is particularly effective against Gram-negative bacteria (Figure 5) [67,68].

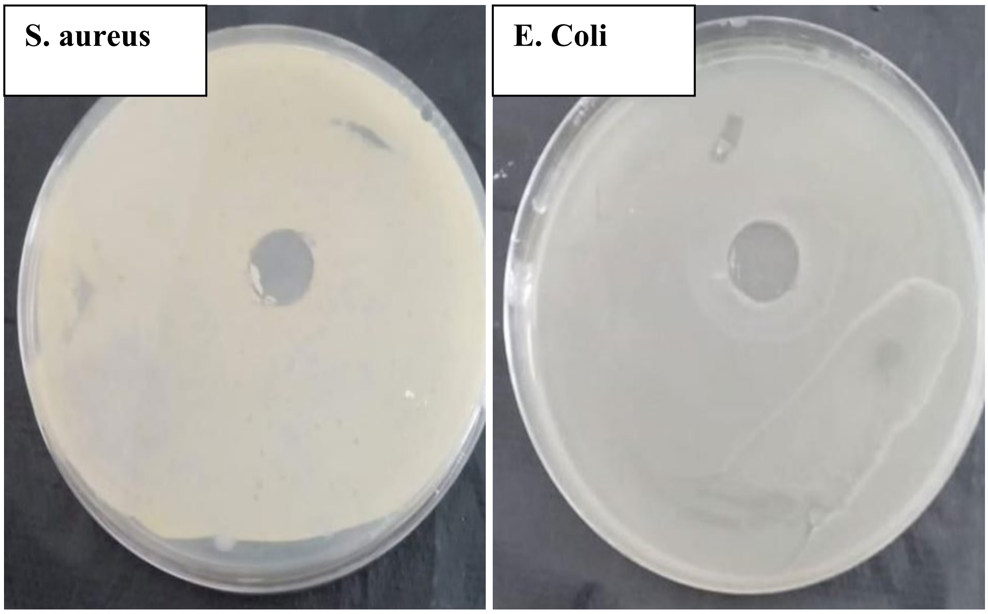

Figure 5 Antibacterial activity of α-Bi_2O_3 pellet calcined at 500 °C against *Staphylococcus aureus* (Gram-positive) and *Escherichia coli* (Gram-negative) by the agar diffusion method (ADM)

3.4.2 SPM

Figure 6 illustrates the antibacterial activity of α-Bi_2O_3 pellets calcined at 500 °C evaluated using the Spread Plate Method (SPM) against *Staphylococcus aureus* and *Escherichia coli*. A clear difference in bacterial survival is observed between the two strains. The surviving colony count for *S. aureus* (Gram-positive) is relatively higher, indicating lower antibacterial effectiveness, whereas *E. coli* (Gram-negative) exhibits a markedly greater reduction in viable colonies, demonstrating stronger antibacterial activity [69, 70]. The enhanced susceptibility of *E. coli* can be attributed to its thinner peptidoglycan layer and the presence of an outer membrane rich in lipopolysaccharides, which promotes oxidative stress damage and facilitates interaction with the α-Bi_2O_3 surface [71]. In contrast, the thicker peptidoglycan layer of *S. aureus* acts as a protective barrier, reducing surface interaction and slowing cell disruption [72]. These findings are consistent with the agar diffusion results and confirm that α-Bi_2O_3 pellets calcined at 500 °C exhibit superior antibacterial efficacy against Gram-negative bacteria, likely due to enhanced crystallinity and surface-driven ROS generation [73-76].

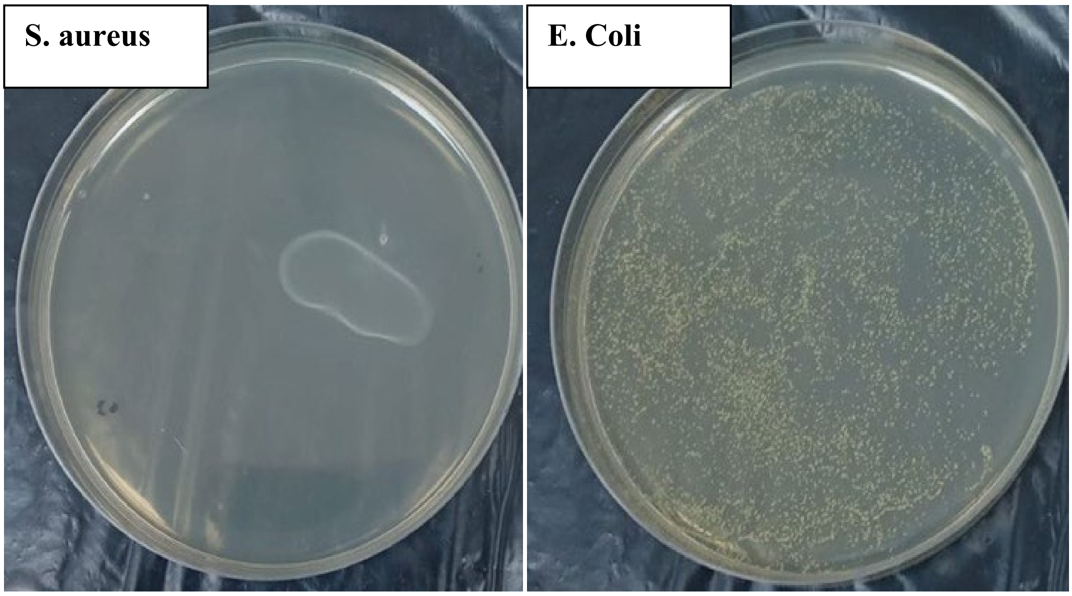

Figure 6 Antibacterial activity of α-Bi_2O_3 pellet calcined at 500 °C against *S. aureus* (Gram-positive) and *E. coli* (Gram-negative), determined using SPM

3.4.3 Statistical comparison for another testing of ADM and SPM results

The antibacterial activity of α-Bi_2O_3 pellets calcined at 500 °C is further assessed using both the Agar Diffusion Method (ADM) and the Spread Plate Method (SPM) against Escherichia coli (Gram-negative) and Staphylococcus aureus (Gram-positive). In ADM, antibacterial performance is evaluated by measuring inhibition zone diameters (mm), whereas in SPM, the effectiveness is determined by counting the surviving bacterial colonies (colony-forming units, CFU). For E. coli, ADM inhibition zones are recorded as 8, 10, and 12 mm, giving a mean value of 10.0 ± 2.0 mm. Correspondingly, SPM colony counts are 3, 5, and 2 colonies, resulting in a mean of 3.33 ± 1.53 colonies. Statistical analysis using a paired t-test revealed a highly significant difference ($t = 6.24$, $p = 0.0033$), confirming that ADM detected a markedly greater antibacterial effect than SPM for this Gram-negative strain. For S. aureus, ADM inhibition zones measured 9, 10, and 13 mm, yielding a mean of 10.67 ± 2.08 mm, while SPM colony counts are 100, 50, and 10, with a mean of 53.33 ± 45.09 colonies. The t-test also showed a statistically significant difference ($t = 3.29$, $p = 0.0291$), indicating that ADM results suggested higher antibacterial activity compared to the colony-based SPM results. The data demonstrate that the choice of antibacterial testing method can substantially influence the measured efficacy, with ADM generally showing stronger apparent inhibition than SPM. This effect is more pronounced for E. coli, likely due to its thinner peptidoglycan layer and greater susceptibility to diffusion-based inhibition, while S. aureus exhibited more resistance, consistent with its thicker cell wall structure (see Table 2).

Table 2 Statistical comparison between the Agar Diffusion Method (ADM) and Spread Plate Method (SPM) in evaluating the antibacterial activity of α-Bi_2O_3 pellets calcined at 500 °C against *E. coli* and *S. aureus*. Values are presented as mean ± standard deviation (SD) based on three replicates, with corresponding *t*- and *p*-values from independent two-tailed Student's *t*-tests. A *p*-value < 0.05 indicates a statistically significant difference between the two methods.

Bacteria	ADM Zoom (mm)			ADM Mean Â± SD	CFU count or colonies			SPM Mean Â± SD	t-value	p-value
E. coli	8	10	12	10.00 ± 2.00	3	5	2	3.33 ± 1.53	6.24	0.0033
S. aureus	9	10	13	10.67 ± 2.08	100	50	10	53.33 ± 45.09	3.29	0.0291

4 CONCLUSIONS

The combined structural, vibrational, magnetic, and antibacterial investigations of α-Bi_2O_3 pellets calcined at different temperatures demonstrate a strong correlation between thermal treatment, crystallinity, and functional performance. XRD analysis confirmed the formation of single-phase monoclinic α-Bi_2O_3 (JCPDS No. 71-0465) for all samples, with no secondary phases detected. As the calcination temperature increased from 300 °C to 500 °C, a systematic reduction in FWHM was observed, accompanied by an increase in crystallite size from 267.83 nm to 373.65 nm, a decrease in microstrain from 3.687×10^{-3} to 2.637×10^{-3}, and a significant drop in dislocation density from 0.14×10^{14} m^{-2} to 0.07×10^{14} m^{-2}, indicating improved crystal quality and reduced defect concentration. FTIR spectra further supported these findings by showing sharper and more intense Bi–O vibrational bands at higher calcination temperatures, reflecting enhanced lattice ordering and phase stability. Magnetic measurements performed using VSM on the sample calcined at 500 °C revealed a narrow hysteresis loop with low coercivity and small remanent magnetization, confirming soft magnetic behavior with weak ferromagnetic characteristics. This magnetic response is attributed to defect-related phenomena such as oxygen vacancies and uncompensated surface spins rather than intrinsic ferromagnetism, and it persists despite the improved crystallinity achieved at higher calcination temperatures. Antibacterial studies showed that α-Bi_2O_3 pellets calcined at 500 °C exhibit effective antibacterial activity against both *Escherichia coli* and *Staphylococcus aureus*. Agar diffusion measurements showed inhibition zones of 10 mm for *E. coli* and 10 mm for *S. aureus*, while spread plate analysis revealed significantly lower bacterial survival for *E. coli* (3 colonies) compared to *S. aureus* (53 colonies). Statistical analysis confirmed significant antibacterial differences ($p = 0.0033$ for *E. coli* and $p = 0.0291$ for *S. aureus*). Overall, the results indicate that higher calcination temperatures enhance the structural quality of α-Bi_2O_3 and promote defect-mediated magnetic behavior, while simultaneously improving antibacterial efficacy, particularly against Gram-negative bacteria due to enhanced surface reactivity and cell wall susceptibility.

REFERENCES

[1] S. Synthiya, T. Thilagavathi, R. Uthrakumar, M. Alam, K. Kaviyarasu, Luminescence, 40 (2025) 77 https://doi.org/10.1002/bio.70161
[2] Z. Chuan et al., J. Alloy. Compound. 4 (2025) 180163 https://doi.org/10.1016/j.jallcom.2025.180163
[3] E.O. Echeweozo, Mine Kırkbınar, Sultan Alomairy, M.S. Al-Buriahi, J. Radia. Resear. Appl. Sci. 18 (2024) 101247 https://doi.org/10.1016/j.jrras.2024.101247
[4] R. Ma et al., Separ. Purif. Tech. 354 (2025) 128580 https://doi.org/10.1016/j.seppur.2024.128580
[5] S. Yang, S. Chen, C. Zhi, Electroch. Ener. Stor. Dev. 2 (2025) 203 https://doi.org/10.1002/9783527834815.ch8
[6] X. Li et al., Sensor. Actu. B Chem., 422 (2024) 136628 https://doi.org/10.1016/j.snb.2024.136628

[7] J. Liu et al., Nanomaterial., 15 (2025) 129 https://doi.org/10.3390/nano15020129
[8] N. Wang et al., J. Alloy. Compound. 1020 (2025) 179493 https://doi.org/10.1016/j.jallcom.2025.179493
[9] V. Ruiz-Santoyo, S. García-Carvajal, M. C. J. Nanopar. Resear., 27 (2025) 1 https://doi.org/10.1007/s11051-024-06207-9
[10] N. Baig et al., Material. Adv., 1 (2021) 335 https://doi.org/10.1039/d0ma00807a
[11] Z. Alhalili, Mater. Today Comm., 1 (2023) 202 https://doi.org/10.1016/j.mtcomm.2023.105809
[12] E. Fazio et al., Sensors, 21 (2021) 2494 https://doi.org/10.3390/s21072494
[13] P. C. D. Mendes, J. Nanopart. Res. 1 (2023) 111 https://doi.org/10.1080/23746149.2023.2175623
[14] V. Mane et al. J. Photochem. Photobiol. B, 2 (2024) 22 https://doi.org/10.1016/j.jphotobiol.2024.112345
[15] C. E. Mohn et al. Phys. Rev. Lett. 102 (2009) 155502 https://doi.org/10.1103/PhysRevLett.102.155502
[16] R. Punn, J. Am. Chem. Soc., 1 (2006) 11 https://doi.org/10.1021/ja065961d
[17] I. Jeong et al., Nanotech. 3 (2022) 27 https://doi.org/10.1038/s41427-022-00402-7
[18] S. F. Wang, Solid State Ion., 1 (2012) 1 https://doi.org/10.1016/j.ssi.2011.10.017
[19] E. Öztürk, Bull. Mater. Sci., 4 (2025) 1 https://doi.org/10.1007/s12034-025
[20] V. Mane et al., Sci. Adv. Mat., 1 (2024) 1 https://doi.org/10.1016/j.sams.2023.12.001
[21] A. R. Khan et al., ACS Omega, 9 (2024) 1234 https://doi.org/10.1021/acsomega.3c10521
[22] S. Tabassum et al., J. Appl. Sci. 1 (2025) 1 https://doi.org/10.1016/j.jtusci.2025.01.009
[23] M. G. Yañez-Cruz et al., J. Analy. Sci. Tech. 13 (2022) 567 https://doi.org/10.1186/s40543-022-00355-0
[24] C. L. Gómez, J. Solid State Ion. 260 (2014) 211 https://doi.org/10.1016/j.ssi.2013.12.012
[25] A. J. Lovett et al., J. Mater. Chem. A 10 (2022) 3478 https://doi.org/10.1039/D1TA07308G
[26] C. E. Mohn et al., Phys. Rev. Lett. 102 (2009) 155502 https://doi.org/10.1103/PhysRevLett.102.155502
[27] R. Punn, J. Am. Chem. Soc. 128 (2006) 5468 https://doi.org/10.1021/ja065961d
[28] I. Jeong et al., Nature, 613 (2022) 695 https://doi.org/10.1038/s41427-022-00402-7
[29] S. Sanna et al., Natur. Mater. 14 (2015) 208 https://doi.org/10.1038/nmat4266
[30] H. Oudghiri-Hassani et al., Tuni. J. Sci. 3 (2015) 127 https://doi.org/10.1016/j.jtusci.2015.01.009
[31] A. C. Gandhi et al., Nanomater. 10 (2020) 100 https://doi.org/10.3390/nano10010100
[32] M. T. Ayala-Ayala et al., ACS Appl. Nano Mater. 8 (2025) 4567 https://doi.org/10.1021/acsanm.4c07108
[33] P. Shuk, Solid State Ion., 87 (1996) 45 https://doi.org/10.1016/0167-2738(96)00348-7
[34] B. Schwaighofer et al., Chemis. Mater., 35 (2023) 3250 https://doi.org/10.1021/acs.chemmater.2c03103
[35] V. Ruiz-Santoyo et al., J. Nanopartic. Res. 27 (2025) 100 https://doi.org/10.1007/s11051-024-06207-9
[36] I. Alshalal, H. M. I. Al-Zuhairi, A. A. Abtan, M. Rasheed, M. K. Asmail. J. Mech. Behav. Mater. 32 (2023) 1 https://doi.org/10.1515/jmbm-2022-0280
[37] M. Sellam, M. Rasheed, S. Azizi, T. Saidani. Ceram. Int. 50 (2024) 20917 https://doi.org/10.1016/j.ceramint.2024.03.094
[38] O. Alabdali, S. Shihab, M. Rasheed, T. Rashid. 3rd inter. Scient. conf. alkafeel univ. (ISCKU 2021) (2022) https://doi.org/10.1063/5.0066860
[39] M. Rasheed, O. Alabdali, S. Shihab, A. Rashid, T. Rashid, J. Phys.: Conf. Ser. 1999 (2021) 1 012078. https://doi.org/10.1088/1742-6596/1999/1/012078
[40] N. Assoudi et al. Opt. Quant. Electron. 54 (2022) 9 https://doi.org/10.1007/s11082-022-03927-x
[41] R. Jalal, S. Shihab, M.A. Alhadi, M. Rasheed, J. Phys.: Conf. Ser. 1660 (2020) 1 012090

https://doi.org/10.1088/1742-6596/1660/1/012090
[42] S. Shihab, M. Rasheed, O. Alabdali, A.A. Abdulrahman, J. Phys.: Conf. Ser. 1879 (2021) 022120 https://doi.org/10.1088/1742-6596/1879/2/022120
[43] A. Keziz, M. Heraiz, M. RASHEED, A. Oueslati. Mater Chem. Phys. 325 (2024) 129757 https://doi.org/10.1016/j.matchemphys.2024.129757
[44] D. Kherifi, A. Keziz, M. Rasheed, A. Oueslati. Ceram. Int. 50 (2024) 30175 https://doi.org/10.1016/j.ceramint.2024.05.317
[45] A. Jaber, M. Ismael, T. Rashid, M. A. Sarhan, M. Rasheed, I. M. Sala. Eureka: Phys. Eng. 4 (2023) 29 https://doi.org/10.21303/2461-4262.2023.002770
[46] T. Rashid, M. M. Mokji, M. Rasheed. J. Optics 99 (2024) 123 https://doi.org/10.1007/s12596-024-02080-w
[47] H. K. Aity, E. Dhahri, M. Rasheed. Ceram. Int. 50 (2024) 54666 https://doi.org/10.1016/j.ceramint.2024.10.324
[48] M. Rasheed, S. Shihab, O. Alabdali, A. Rashid, T. Rashid, J. Phys.: Conf. Ser. 1999 (2021) 012077 https://doi.org/10.1088/1742-6596/1999/1/012077
[49] M. Rasheed, M. Nuhad Al-Darraji, S. Shihab, A. Rashid, T. Rashid. J. Phys.: Conf. Ser. 1963 (2021) 012058 https://doi.org/10.1088/1742-6596/1963/1/012058
[50] A. Keziz, M. Heraiz, F. Sahnoune, M. Rasheed, Ceram. Int. 49 (2023) 32989 https://doi.org/10.1016/j.ceramint.2023.07.275
[51] E. Kadri, K. Dhahri, R. Barillé, M. Rasheed. Phase Transi. 94 (2021) 65 https://doi.org/10.1080/01411594.2020.1832224
[52] D. Bouras, M. Rasheed, Opt. Quantum Electron. 54 (2022) 12 https://doi.org/10.1007/s11082-022-04161-1
[53] A. Zubaidi, L.M. Asaad, I. Alshalal, M. Rasheed, J. Mech. Behav. Mater. 32 (2023) 1 https://doi.org/10.1515/jmbm-2022-0302
[54] M. Rasheed et al., J. Phys.: Conf. Ser. 1999 (2021) 012080 https://doi.org/10.1088/1742-6596/1999/1/012080
[55] M. Rasheed, M.N. Al-Darraji, S. Shihab, A. Rashid, T. Rashid, J. Phys.: Conf. Ser. 1963 (2021) 012059 https://doi.org/10.1088/1742-6596/1963/1/012059
[56] M. Enneffatia, M. Rasheed, B. Louati, K. Guidara, S. Shihab, R. Barillé, J. Phys.: Conf. Ser. 1795 (2021) 012050 https://doi.org/10.1088/1742-6596/1795/1/012050
[57] M. Rasheed, O.Y. Mohammed, S. Shihab, A. Al-Adili, J. Phys.: Conf. Ser. 1795 (2021) 012043 https://doi.org/10.1088/1742-6596/1795/1/012043
[58] A.H. Ali, A.S. Jaber, M.T. Yaseen, M. Rasheed, O. Bazighifan, T.A. Nofal, Complexity 2022 (2022) 1 https://doi.org/10.1155/2022/9367638
[59] M. Rasheed, et al., J. Adv. Biotechnol. Exp. Ther. 6 (2023) 495 https://doi.org/10.5455/jabet.2023.d144
[60] M. Rasheed, I. Alshalal, A.A. Ashed, M.A. Sarhan, A.S. Jaber, Indones. J. Electr. Eng. Comput. Sci. 33 (2024) 653 https://doi.org/10.11591/ijeecs.v33.i1.pp653-660
[61] I.M. Mohammed, M. Rasheed, AIP Conf. Proc. 3321 (2025) 020026 https://doi.org/10.1063/5.0289719
[62] F. Boudou, A. Belakredar, A. Berkane, M. Rasheed. Not. Sci. Biol. 17 (2025) 12183 https://doi.org/10.55779/nsb17212183
[63] F. Boudou, et al., Not. Sci. Biol. 17 (2025) 12593 https://doi.org/10.55779/nsb17312593
[64] F. Boudou, A. Guendouzi, A. Belkredar. M. Rasheed, Not. Sci. Biol. 16 (2024) 13837 https://doi.org/10.55779/nsb16211837
[65] R.S. Mahmood et al. J. Mech. Behav. Mater. 34 (2025) 1 https://doi.org/10.1515/jmbm-2025-0040
[66] T. Rashid, M.M. Mokji, M. Rasheed, J. Mech. Behav. Mater. 34 (2025) 77 https://doi.org/10.1515/jmbm-2025-0074
[67] M. Rasheed, M. N. Mohammedali, F. A. Sadiq, M. A. Sarhan, T. Saidani. J. Optics (New Delhi.

Print) (2024). https://doi.org/10.1007/s12596-024-01928-5

[68] A.J. Hussein, M.N. Al-Darraji, M. Rasheed, M.A. Sarhan, IOP Conf. Ser.: Earth Environ. Sci. 1262 (2023) 022007 https://doi.org/ 10.1088/1755-1315/1262/2/022007

[69] A.J. Hussein, M.N. Al-Darraji, M. Rasheed, M.A. Sarhan, IOP Conf. Ser.: Earth Environ. Sci. 1262 (2023) 022005 https://doi.org/10.1088/1755-1315/1262/2/022005

[70] T. Saidani, M. Rasheed, I. Alshalal, A.A. Rashed, M.A. Sarhan, R. Barillé, Res. Eng. Struct. Mater. 10 (2024) 743 http://dx.doi.org/10.17515/resm2023.21ma0922rs

[71] S.A. Hayder, et al. ARPN J. Eng. Appl. Sci. or ARPN-JEAS. 13 (2018) 2395 https://doi.org/10.1109/access.2020.2983149

[72] H. S. Ahmed, A. J. Salim, J. K. Ali, M. A. Alqaisy, 5 (2016) 1 https://doi.org/10.1109/mms.2016.7803836

[73] H. S. Ahmed, A. N. Almamori. Progress In Electromagnetics Research C 154 (2025) 159 https://doi.org/10.2528/pierc25021810

[74] Rida Ahmed Ammar, Experimental and Theoretical NANOTECHNOLOGY 2 (2018) 1 https://doi.org/10.56053/2.1.1

[75] M. Mourad Mabrook, Experimental and Theoretical NANOTECHNOLOGY 2 (2018) 103 https://doi.org/10.56053/2.2.103

[76] F. M. Shamsudin, S. Radiman, Y. Abdullah, N. A. Hamid, Experimental and Theoretical NANOTECHNOLOGY 3 (2019) 27 https://doi.org/10.56053/3.1.27